This is a post-peer-review, pre-copyedit version of an article published in Indraratna, B., Haq, S., Rujikiatkamjorn, C. et al. Microscale boundaries of internally stable and unstable soils. Acta Geotech. 17, 2037–2046 (2022). The final authenticated version is available online at: https://doi.org/10.1007/s11440-021-01321-7

Hydromechanical State of Soil Fluidisation – Mircoscale Perspective

Shay Haq

BEng (Hons)

PhD Candidate, Transport Research Centre, University of Technology Sydney, NSW 2007. Australia.

Buddhima Indraratna[1]

PhD (Alberta), MSc (Lond.), BSc (Hons., Lond.), DIC, FTSE, FIEAust., FGS, CEng, CPEng

Distinguished Professor of Civil Engineering, Director of Transport Research Centre, School of Civil and Environmental Engineering, University of Technology Sydney, NSW 2007, Australia.

[1]Corresponding author e-mail: buddhima.indraratna@uts.edu.au

Thanh Trung Nguyen

PhD, MEng (Saitama), BEng (Hons), CPEng, M. ASCE

Research Fellow, Transport Research Centre, School of Civil and Environmental Engineering, University of Technology Sydney, NSW 2007, Australia.

Cholachat Rujikiatkamjorn

PhD, MEng (AIT), BEng (Hons)

Professor, Transport Research Centre, School of Civil and Environmental Engineering, University of Technology Sydney, NSW 2007, Australia.

Words: 5015

Figures: 14

Tables: 1

Abstract

This paper investigates soil fluidisation at the microscale using the Discrete Element Method (DEM) in combination with the Lattice Boltzmann Method (LBM). Numerical simulations were carried out at varying hydraulic gradients across the granular assembly of soil, and the development of localised hydraulic gradients, the contact force distribution, and the associated fabric changes were investigated. The novelty of this study includes microscale findings which suggest that a critical hydromechanical state inducing fluid-like instability of a granular assembly can initiate when substantial increase in grain slipping associated with reduced interparticle contacts suddenly occur. Based on these results, a new micro-mechanically inspired criterion is proposed to characterise the transformation of granular soil from a stable solid phase to an hydromechanically unstable state. The constraint ratio (number of constraints in relation to the degrees of freedom) is introduced to portray the relative slip between particles and the loss of interparticle contacts within the granular fabric. Its magnitude of unity corresponds to the condition of zero effective stress, representing the critical hydromechanical state. In a practical sense, the results of this study reflect the phenomenon of subgrade mud pumping that occurs in railways upon the passage of heavy haul trains at certain axle loads and speeds.

Keywords: Fluidisation, Discrete Element Method, Lattice Boltzmann Method, Constraint Ratio, Critical Hydraulic Gradient

==

1. Introduction

A major problem leading to railroad instability that creates immense maintenance costs is related to the degradation of the soft subgrade and its potential for fluidisation or mud-pumping [1-5]. In this context, fluidisation is defined as when saturated soils are exposed to excessive hydraulic gradients and lose their intergranular contacts to transition into a fluid-like state. As a result, this slurry of fine particles migrates (pumps) into the overlying coarser ballast layer, hence the commonly used term mud-pumping, as investigated experimentally [2, 4, 6]. These laboratory tests enable a better understanding of the hydromechanical behaviour of the subgrade soils, but primarily at the macroscale. From a micromechanical perspective, i.e., at the grain level, slippage and/or breakage of the interparticle contacts and the resulting fabric evolution may initiate the transition from a hydromechanically stable to an unstable state that is still not fully understood.

The Discrete Element Method (DEM) is a useful tool for assessing the micromechanics of a granular medium [7, 8] that has been effectively used to study the evolution of interparticle contacts and fabric during shear using the scalar and directional parameters [9, 10]. The coordination number (number of contacts per particle in the granular assembly) is a fundamental microscale fabric descriptor for characterising granular medium [10, 11]. Nonetheless, the state of interparticle contacts and fabric during fluid flow has rarely been considered. In addition, the constraint ratio, defined by the ratio of the number of constraints to the number of degrees of freedom within the particle system [12], can be used to represent the relative slip and loss of interparticle contacts during instability. However, none of past DEM studies have defined any quantitative parameters to describe the rational mechanisms of soil fluidisation in contrast to more commonly observed undrained failures of saturated soils.

The primary scope of this paper includes an attempt to describe and quantify the critical hydromechanical conditions corresponding to the fluidisation phenomenon with special attention to granular soil at the microscale, adopting the concepts of the coordination number and the constraint ratio, as mentioned above. For the first time, a comprehensive assessment of different microscale aspects in relation to fluidisation is introduced in the current study, including an original micro-condition representing the inception of hydraulic failure of a saturated soft subgrade. Indeed, the DEM can be used in combination with Computational Fluid Dynamics (CFD) to study internal erosion and soil fluidisation in detail [13-16]. Neither of these studies could accurately quantify the critical hydromechanical conditions leading to potential fluidisation from a microscale perspective, so a more insightful microscale study of this instability process is needed.

Given the above, this study uses a combined fully resolved LBM-DEM approach that is becoming increasingly popular to study fluid-particle interactions [17-19]. The advantages of the fully resolved approaches over unresolved approaches include (a) the ability to produce a much finer mesh size, i.e., finer than the particles that can simulate true experimental conditions, (b) a higher computational speed when run on parallel computers and, (c) the relative feasibility of implementation in complex geometries of porous media [20, 21]. In addition, the LBM is based on the kinetic theory of gases and represents a fluid through an assembly of particles that go through successive collision and propagation processes. This enables the calculation of the macroscopic fluid velocity and the pressure as a function of the momentum of these particles [21, 22].

The application of micromechanical modelling to a given volume of a porous medium will have inevitable size-effects when compared to real-life analysis. In the field, the seepage path lengths are large (e.g. several meters in dam sites, landslide areas etc.) compared to small-scale laboratory specimens, so one would expect the measured hydraulic gradients to be significantly smaller and generally less than unity [23]. In contrast to FEM and FDM analyses based on continuum mechanics for larger soil domains, the DEM analysis often becomes inefficient in terms of computational time when a large soil volume is considered. As a result, for convergence of output to an acceptable accuracy, only a limited soil area can be usually analysed using DEM, hence the computed hydraulic gradients tend to be larger [24-26].

Lattice Boltzmann Method (LBM) combined with Discrete Element Method (DEM)

The theoretical formulations of the LBM-DEM approach are described as follows:

2.1 Fluid equations

The governing Boltzmann equation is written as [27]:

$$\frac{\partial f_\alpha(x,t)}{\partial t} + e_\alpha^v \, \nabla f_\alpha(x,t) = \Omega_\alpha \qquad (\alpha = 1,2, \dots \dots \dots .., N) \tag{1}$$

where $f_\alpha(x,t)$ is the particle distribution function in the α direction, e_α^v is the microscopic fluid velocity and Ω_α is the collision operator, and t is the time. Equation (1) can be discretised on a regular lattice using a unique finite difference method, and the lattice-Boltzmann equation with the Bhatnagar-Gross-Krook (BGK) collision operator for a Newtonian fluid is written as [27, 28]:

$$f_\alpha(x + e_\alpha^v \, \Delta t, t + \Delta t) - f_\alpha(x,t) = {\Omega_\alpha}^{BGK} \tag{2}$$

where ${\Omega_\alpha}^{BGK}$ is the BGK collision operator, and Δt is the time-step.

Each time step is divided into two sub-steps, i.e., the collision and streaming step, and the collision step is written as:

$$f_\alpha(x,t^*) = f_\alpha(x,t) + {\Omega_\alpha}^{BGK} \tag{3}$$

$f_\alpha(x,t^*)$ and $f_\alpha(x,t)$ are the particle distribution functions after and before the collision, respectively, and t^* is the time after the collision. In the streaming step, the $f_\alpha(x,t^*)$ is propagated over the lattice grid as follows:

$$f_\alpha(x + e_\alpha^v \, \Delta t, t + \Delta t) = f_\alpha(x, t^*) \tag{4}$$

2.2 Fluid-particle interaction

The participation of solid particles in the fluid is achieved by introducing an additional collision term (Ω_α^s) in Equation (3) as suggested by Noble & Torczynski (1998) [29]:

$$f_\alpha(x, t^*) = f_\alpha(x, t) + [1 - B\,]{\Omega_\alpha}^{BGK} + B{\Omega_\alpha}^{s} \tag{5}$$

$$B = \frac{\varepsilon_s\left({}^{\tau}/_{\Delta t} - {}^{1}/_{2}\right)}{(1 - \varepsilon_s) + \left({}^{\tau}/_{\Delta t} - {}^{1}/_{2}\right)} = (0,1) \tag{6}$$

where ε_s is the solid fraction in the fluid cell volume, B is a weighting function for correcting the collision phase of the lattice-BGK equation due to the presence of solid particles, and τ is the relaxation time (Appendix 1). The method for calculating the solid fraction for the moving particles is described by [22].

The non-equilibrium part of the particle distribution function is bounced back and ${\Omega_\alpha}^s$ is computed using:

$${\Omega_\alpha}^{s} = f_{-\alpha}(x, t) - f_\alpha(x, t) + {f_\alpha}^{eq}\left(\rho_f, v^p\right) - {f_{-\alpha}}^{eq}\left(\rho_f, u\right) \tag{7}$$

where v^p is the velocity of solid particle p at time $t + \Delta t$ at the node, u is the macroscopic fluid velocity, and the notation $f_{-\alpha}$ is the rebound state obtained by reversing all microscopic fluid velocities, i.e., e_α^v to $e_{-\alpha}^{v}$. Further details on the fluid equations and the fluid-particle interaction are described in Appendix A.

2.3 Validation

Figure 1 shows the flowchart of the LBM-DEM approach described above. The DEM calculation cycles are within the LBM cycles. In order not to impair the accuracy of the simulation, a suitable interval for the information exchange between 2 phases was chosen [30].

Although the coupled LBM-DEM approach was previously validated by Indraratna et al. (2021a) [18] with experimental observations of fluidisation, the transient motion of the particles in the fluid was not quantified. In this regard, this study attempts to validate the motion of a single particle falling into the fluid with different particle Reynold's numbers (Re_p). This validation is carried out by comparing the numerical results with the experimental observations by Ten Cate et al. (2002) [31]. Figures 2(a) and 2(b) show the schematic sketch and the modelled problem using the LBM-DEM approach, respectively. Table 1 shows the fluid properties used with lattice resolution (N) = 5 (particle diameter corresponds to 5 fluid cells) and the relaxation time (τ) = 0.53. It is noteworthy that $N = 5$ was chosen after a preliminary sensitivity analysis in which the simulation was run with $N = 5$, 7 and 10. The results showed insignificant difference in the numerical output when $N > 5$. Figures 2(c) and 2(d) show an excellent agreement between the numerical and experimental results of the position and velocity of the falling particle over time at different Reynold's numbers. Hence, it could be justified with confidence that the LBM-DEM approach would reasonably predict the transient motion of the particles in the fluid with these selected numerical parameters.

2. Simulating Soil Specimen Fluidisation

3.1 Simulation approach

Three-dimensional LBM-DEM simulations were carried out using the Hertz-Mindlin contact model (Appendix B) with the Young's modulus and the Poisson's ratio of the particles as 70 GPa and 0.3, respectively (Thornton, 2000). The particle density was set to 2650 kg/m^3, and the rigid boundary walls were used. The gravitational deposition method was used for sample preparation [32], whereby the acceleration due to the force of gravity of the particles was set to 9.81 m/s^2. The particles were initially created in a larger volume with no overlap and then dropped under gravity. The particles were allowed to settle until equilibrium was reached, thereby ensuring that the coordination number remained constant for a sufficient number of numerical cycles. The sample was prepared in a dense state by setting the coefficient of friction (μ_s) to 0 [32, 33]. Subsequently, μ_s was changed to 0.30, and the particles were re-equilibrated with a sufficient number of numerical cycles before the particles became saturated with the fluid. The μ_s value used in this study is in the range of real quartz particle values that can be determined experimentally with a micromechanical interparticle loading apparatus [34]. It is assumed that the particle-wall contact parameters correspond to the particle-particle contact parameters [35, 36].

The fluid density was set to 1000 kg/m^3 with a kinematic viscosity of 1 x 10^{-6} m^2/s according to pure water properties at 20 ºC and 1 atmosphere (101 kPa). The resolution of the fluid lattice was chosen with at least 5 lattices in each particle, i.e., the smallest particle diameter corresponds to at least 5 fluid cells with regard to the validation of the single-particle displaced downwards into the fluid described previously. A relaxation parameter close to but greater than 0.50 was chosen, and the Mach number was kept below 0.1, inspired by the need for improved accuracy, as explained elsewhere by Han et al. (2007) [20]. The fluid flow was initiated with the relevant inlet and outlet pressure boundary conditions, and no-slip conditions were imposed on the boundaries perpendicular to the flow. For each hydraulic gradient applied, the flow was continued over a sufficient period of time until a steady-state condition was attained.

3.2 Particle size distribution and homogeneity of the sample

Figure 3(a) shows the particle size distribution of the selected sample from an experimental study carried out earlier by Indraratna et al. (2015) [24]. Figure 3(b) shows the three-dimensional DEM-based sample with 17607 particles, and the direction of fluid flow is also shown, i.e., the *z*-direction. Figure 3(c) shows the division of the sample into 10 different inner layers. The ratio of the lateral dimension of the simulation domain to the maximum particle diameter was kept greater than 12 in order to obtain a representative elementary volume (REV) and avoid the boundary effects. A local decrease in the void ratio occurs near the rigid boundaries [8]; hence, the bottom boundary layer (besides the rigid bottom boundary) was neglected in order to nullify the boundary effects [37]. The thickness of each layer was chosen to be more than twice the maximum particle diameter to define a REV [37]. The stresses at the boundaries do not reflect the actual material response; therefore, the interaction of the particles in each layer with the lateral boundaries was not taken into account.

Figure 3(c) shows the similar initial void ratios of all layers, indicating the REV in each layer, and the initial homogeneity of the sample was further confirmed by considering the variances in the void ratios as reported by Jiang et al. (2003) [38]:

$$S^2 = \frac{1}{n_L - 1} \sum_{k=1}^{n_L} (e_{oi}^k - e_{oi}^{avg})^2 \tag{8}$$

where S is the variance of the void ratios, n_L is the total number of layers, e_{oi}^k is the initial void ratio of the k^{th} layer, and e_{oi}^{avg} is the initial void ratio of the entire sample. The S^2 value for the sample in Fig. 3(c) is 2.72 x 10^{-5}, which is sufficiently low to classify the sample as homogenous with respect to the REV in each layer. The overall void ratio of the numerical sample is the same as that of the experimental sample. Note that the void ratio does not take into account the particulate structure of the granular medium. Figure 3(d) shows a close-up view of the particles modelled in the fluid mesh. It can be seen that the mesh size is much smaller than the particle and pore size, in contrast to the conventional unresolved approach with the Navier-Stokes equation.

3.3 Calibration

Figure 4 shows the calibration of the numerical model of soil fluidisation by comparing the flow curves obtained from the LBM-DEM approach and those of an earlier experimental study

(Indraratna et al., 2015) [24]. The flow curves obtained from the LBM-DEM approach and the experimental study agree with each other. The overall hydraulic gradient (i_o) is derived from the pressure difference between the top and bottom of the specimen, i.e., $i_o = \Delta P/\gamma_w L$, where γ_w is the unit weight of water. The overall critical hydraulic gradient ($i_{o,cr}$) predicted by the LBM-DEM approach was 1.050 and the experimental value was 1.180. These values are in acceptable agreement with one another.

It is important to note that the values of $i_{o,cr}$ predicted by the current LBM-DEM approach and the previous authors' experimental studies [24] are larger than the theoretical values based on the upward flow heave phenomenon (i.e., zero effective stresss) described by Tezaghi [39]. This is because such classical therories ignore interparticle friction within the microscale soil fabric, and also assumefrictionless boundaries in the analysis. In contrast, the current DEM simulation considered a friction coefficient of 0.3 for the wall-particle interaction as well as interparticle contacts, resulting in an increase of the critical hydraulic gradients in the micromechanical fluid-particle coupled approach. The current computational results for hydraulic gradients are in agreement with several past micromechanical and experimental studies [25, 26, 36].

3. Results and Discussion

4.1 Stress-hydraulic gradient evolution

Figure 5 shows the stress-hydraulic gradient space where the local hydraulic gradients (i_{hyd}) are plotted against the normalised Cauchy effective stresses ($\sigma'_{zz}/\sigma'_{zzo}$) of particles in a given layer in the fluid flow direction at any time. Here, σ'_{zz} is the Cauchy effective stresses of the particles in a layer at any time, and σ'_{zzo} is the initial Cauchy effective stresses of the particles in that particular layer. The local hydraulic gradients are computed based on the pressure difference across each layer, i.e., $i_{hyd} = \Delta P_{layer}/\gamma_w L_{layer}$, where ΔP_{layer} is the pressure drop across the layer and L_{layer} is the thickness of each layer. The σ'_{zz} is obtained using the particle-based stresses via the following second-order stress tensor equation [40].

$$\sigma'_{ij} = \frac{1}{V} \sum_{p=1}^{N_p} \sigma_{ij}^{p\prime} V^p \tag{10}$$

where V is the volume of the layer or the selected region, V^p is the volume of particle p in the region, N_p is the number of particles in the layer, and $\sigma_{ij}^{p\prime}$ is the average stress tensor within a particle p and is given by:

$$\sigma_{ij}^{p\prime} = \frac{1}{V^p} \sum_{c=1}^{N_c^p} \left| x_i^c - x_i^p \right| n_i^{c,p} f_j^c \tag{11}$$

where f_j^c is the force vector in the j^{th} direction at contact c with the location x_i^c, x_i^p is the location of the particle's centroid, $n_i^{c,p}$ is the unit normal vector from the particle's centroid to the contact location and N_c^p is the number of contacts on the particle p. Note that Equations (10) and (11) compute the effective stresses directly from the contact moments and not according to the Terzaghi's concept used in the macroscale laboratory studies. Reynold's stresses are negligible up to the beginning of fluidisation and are not taken into account.

The onset of fluidisation of the soil is associated with hydraulic and stress conditions, i.e., the hydromechanical conditions. The effective stresses decrease with increasing local hydraulic gradients in each layer. The onset occurs at a critical hydraulic gradient when the effective stresses drop to zero. The evolution of the stress-gradient of each layer is not the same. The stress-gradient paths of Layers 1-6 are approximately linear with a slope of -1. In contrast to the theoretical linear stress-gradient paths presented by Li and Fannin (2012) [41], the stress-gradient paths of Layers 7-10 (lower layers) are nonlinear until failure. The failure initiates when the effective stress of Layer 10 approaches zero. At the same time, Layers 1-9 show residual stresses due to the motion of the particles in the form of clusters. These residual stresses decrease as the particles in the cluster would lose further contacts over time after onset until complete fluidisation occurs.

4.2 Broken contacts

Figure 6 shows the development of the broken contacts (B_R) compared to the normalised effective stresses ($\sigma'_{zz}/\sigma'_{zzo}$). B_R is the percentage of interparticle contact losses in the initial number of contacts in the corresponding layer. The value of B_R increases with increasing hydraulic gradient and decreasing effective stresses. Contact is lost when the normal contact force due to hydrodynamic forces becomes zero. When the fluid flows, the contacts break off, and new contacts are also formed in the layer. The sharp drop in B_R represents the critical hydromechanical state where the contacts are notably lost. The granular assembly would become a fully fluid-like material when the number of unconnected particles increases to the maximum due to the breakage of the contacts. In other words, most of the particles would simply float without any contact. It can also be seen that the contact losses in the lower layers are greater than in the upper layers, which shows that more particles lose contact at the bottom and migrate upwards with the fluid flow if the constrictions are wide enough. The value of B_R at the critical hydraulic gradient is about 5% in Layer 1 and 17% in Layer 10, and it increases considerably with a further slight increase in the hydraulic gradient applied across the soil specimen.

4.3 Mechanically stable particles

Figure 7 shows the evolution of the fraction of mechanically stable particles (M_s) with normalised effective stresses ($\sigma'_{zz}/\sigma'_{zzo}$) under increasing hydraulic gradients. The mechanically stable particles are those that participate in the stable network of force transmission. The value of M_s is defined by [42]:

$$M_s = \frac{N_p^{\geq 4}}{N_p} \quad (12)$$

where $N_p^{\geq 4}$ is the number of particles with at least 4 or more contacts. Particles with zero contacts that do not participate in the stable network of force transmission are called rattlers or unconnected particles; hence, they are excluded. The particles with 1, 2, and 3 contacts are temporarily stable for a limited time, so they are also neglected in the above equation.

It should be noted that the values of M_s are always smaller than 1 across all layers since the temporarily stable particles are also present at the hydrostatic state. The initial values of M_s are higher in the lower layers than in the upper layers. The values of M_s decrease across all layers with a reduction in the magnitude of effective stresses. This reduction becomes significant at the critical hydraulic and stress conditions that indicate the breakup of the clusters of mechanically stable particles. The results show that a critical value of $M_s \approx 0.75$ is found for all layers, below which the fluid-like behaviour of the soil is observed.

4.4 Evolution of the soil fabric

Figure 8 shows a conceptual model that describes the differences in the fabrics of two-particle systems where particles with two different geometrical arrangements are placed, where the void ratios of both arrangements are the same. However, the number of interparticle contacts is different due to the dissimilarity of the fabrics of the particulate systems. It is noteworthy that the geometric arrangement of the particles is more important than the void ratio when it comes to the strength of the granular assembly [12]. Similar initial void ratios of all layers indicate that the number of particles in each layer is the same. However, the number of interparticle contacts may vary due to the different geometrical configurations of the particles. During fluid flow, the number of particles in each layer remains unchanged until fluidisation begins, while the geometrical rearrangement of the particles can occur, mainly attributed to the interparticle contacts within the layer slip and/or break.

To assess the evolution of soil fabric under fluid flow, this study uses a scalar approach [11] to quantify the fabric with a scalar fabric descriptor called the coordination number (*Z*) and is computed as follows [10].

$$Z = \frac{2N_c}{N_p} \tag{13}$$

where N_c is the number of contacts and is multiplied by 2 since each contact is shared by two different particles.

Figure 9 shows the distribution of the *Z* at the hydrostatic state and the onset of soil fluidisation, taking into account three distinct cases:

(a) all particles,
(b) particles with diameters (d_p) ≥ d_{50} (where d_{50} is the particle size that is 50% finer by mass), and
(c) particles with $d_p \geq d_{85}$ (where d_{85} is the particle size that is 85% finer by mass)

Figure 9(a) shows that the distribution of the coordination numbers at the hydrostatic state across different layers is somewhat dissimilar when all particles are considered. This difference is enhanced when larger particle sizes are taken into consideration (Figures 9(c) & 9(e)), which is reflected by a dissimilarity in the fabric of all layers despite similar void ratios. This fabric dissimilarity is ascribed to the influence of gravity during the sample preparation phase. The curves of the lower layers are on the right-hand side and show higher values of the coordination numbers than those of the upper layers. The slight difference in the evolution of local hydraulic gradients and effective stresses through each layer, as previously described, is due to this slight dissimilarity of the particles' fabric in the layers. It is appealing to note that at the onset of fluidisation, the distributions of the coordination numbers of all layers converge and become similar (Figures 9(b), 9(d), & 9(f)). The median value of the coordination number (Z_{50}) is 4 when all particles in the granular medium of the layer are taken into account (Figure 9(b)). Thus, at the onset of fluidisation, the distributions of the interparticle contacts are uniform and show a similar fabric for all soil layers.

Figure 10 shows average coordination numbers (Z_{avg}) versus normalised effective stresses ($\sigma'_{zz}/\sigma'_{zzo}$), where the initial (at the hydrostatic state) average coordination of Layer 10 is the highest (i.e., Z_{avg} = 5.405), while Layer 1 has the lowest (i.e., Z_{avg} = 4.811). As the normalised effective stresses decrease, the values of Z_{avg} decrease across all layers, and so does the difference between them. Although each layer initially had a different fabric, the Z_{avg} of all layers has evolved to become the same, i.e., 4.6 at critical hydromechanical state.

4.5 Slipping index

Figure 11 shows the distribution of the slipping index (S_i) of the selected Layer 10. Here, all layers show an almost similar development in the slipping index as the local hydraulic gradient increases. The slipping index (S_i) is defined by [42]:

$$S_i = \frac{f^T}{\mu_s f^N} \tag{14}$$

Slipping or the plastic contacts occur when the tangential contact force (f^T) has fully mobilised the friction, i.e., S_i = 1. The contacts with S_i < 1 are the elastic contacts and f^T is independent of f^N in such contacts. Note that contacts that have already been lost are not taken into account when calculating S_i.

The results show that a small proportion of the contacts slip even at the hydrostatic state, as the static buoyancy forces act on the particles when they are saturated with the fluid. As the local hydraulic gradients increase, the elastic contacts decrease, and the slipping contacts increase. The hydrodynamic forces from the seepage flow tend to move the particles, causing a change in the magnitudes of the resisting tangential contact force and the normal contact force. As a result, a slip is caused when the elastic tangential contact force reaches the Coulomb cut-off, i.e., $f^T = \mu_s f^N$ and this slipping of the particles occurs in the weak contacts ($f^N < f_o^{N,avg}$). At $i_{hyd} \leq 1$, the proportion of slipping contacts in the total number of contacts in the layer is ≤ 10%, while it is around 17% at the critical i_{hyd} =1.251 as shown in Figure 11(g). Thereafter, this proportion of slipping contacts increases steeply with a further, albeit slight, increase in the hydraulic gradient. It is noteworthy that the maximum tangential force is controlled by the value of μ_s. Therefore, the value of μ_s has a profound influence on the proportion of slipping contacts and consequently on the macroscale behaviour of the granular assembly.

4.6 Constraint ratio

Figure 12 shows a three-dimensional representation of the constraint ratio (*R*) versus local hydraulic gradients (i_{hyd}) and normalised effective stresses ($\sigma'_{zz}/\sigma'_{zzo}$). The constraint ratio for a three-dimensional particle system that only takes the sliding resistance into account is given by (Cundall & Strack, 1983):

$$R = \frac{N_{ct}}{N_d} = \frac{N_c(3 - 2S_c)}{6N_p} \tag{15}$$

where N_{ct} is the number of constraints, N_d is the number of degrees of freedom, and S_c is the fraction of slipping contacts in the total number of contacts at a given point in time. For an idealised granular medium with $\mu_s = \infty$, $N_{ct} = 3N_c$ and $N_d = 6N_p$. The realistic granular medium, however, would have a finite value of μ_s; therefore, the two tangential force constraints on contacts subject to slipping vanish and are excluded from the total number of constraints given in equation (15). Theoretically, if $N_{ct} > N_d$, the granular assembly is considered to be over-constrained or mechanically stable, and if $N_{ct} = N_d$, it is considered to be in a critical or transitional state; otherwise, it is unstable. Note that R represents both slipping and loss of contacts in the particle systems, whereas the coordination number does not take into account the slipping of particles [10].

The constraint ratio in each layer decreases according to the nonlinear power laws when the normalised effective stresses decrease, and it decays exponentially after the onset of the soil fluidisation (Fig. 12). The initial mild slope shows that at the relatively low i_{hyd} values, i.e., $i_{hyd} < 1$, the particles slip less and have minimal loss of contacts. The abrupt change in slope after onset is triggered by substantial slipping and the associated rapid loss of interparticle contacts. The point at which the slope value changes represents the critical microscale hydromechanical state or the onset of soil fluidisation. This point is marked as a transition from a hydromechanically stable to a fluid-like state, as shown in Fig. 12(b). This critical hydromechanical state corresponds to $R \approx 1$, with effective stresses ≈ 0 at the critical hydraulic gradient. In this respect, the soil is hydromechanically stable when R is greater than 1, while it is in a transition state from a hydromechanically stable to a fluid-like state when R is 1; otherwise, it corresponds to a slurry or fluid-like state. Complete fluidisation of the soil specimen occurs when almost all interparticle contacts are lost, which is represented by a constraint ratio that is significantly below 1.

4. Conclusions

This study assessed the hydromechanical state of soil fluidisation from a micromechanical perspective using the LBM-DEM approach. The good agreement between the model predictions and the experimental observations in relation to particle motion, fluid flow curves, and the critical hydraulic gradients confirms the capability and reliability of this hybrid numerical method. Based on the findings of this study, the following salient outcomes can be drawn:

- At comparatively low values of the local hydraulic gradient (i_{hyd}), i.e., $i_{hyd} \leq 1$, the proportion of slipping contacts in the total number of contacts of the selected Layer 10 (bottom of the specimen) was ≤ 10%, while it was approximately 17% at the critical i_{hyd} =1.251. The extent of slipping contacts increased with a further increase in the hydraulic gradient applied across the soil specimen.
- The fraction of mechanically stable particles was generally larger at the deeper layers, but decreased with the reduction in normalised effective stress during the corresponding increase in hydraulic gradient. The fluid-like state of soil was triggered when this fraction of mechanically stable particles dropped below 0.75.
- The hydrodynamic forces induced by the seepage flow inevitably destable and move the particles within the granular assembly, also resulting in decreased contact forces, thus creating critical conditions to facilitate particle slipping. The loss of interparticle contacts was not uniform across the depth of the soil specimen, as this was more pronounced in the deeper layers when subjected to an upward flow from the base of specimen.
- At the critical hydraulic gradient, the percentage of interparticle contact losses relative to the initial number of contacts was non-uniform and varied between 5 and 17% across the specimen depth. Thereafter, even with a slight increase in the hydraulic gradients, the breakage of the interparticle contacts appeared to exacerbate.
- At the onset of fluidisation, the distributions of the coordination numbers across all layers of the soil specimen became more uniform, with a median value of 4 and an average value of 4.6, thus representing a more uniform granular fabric across the soil layers.
- The novel use of the constraint ratio to portray soil instability proved that the granular assembly was hydromechanically stable when the constraint ratio > 1 and unstable (fluid-

like) when the constraint ratio < 1, thereby establishing the microscale hydromechanical critical state at the constraint ratio of unity.

Declaration of Competing Interest

The authors state that they are not aware of any competing financial interests or personal relationships that may have influenced the work reported in this paper.

Acknowledgements

The financial support from the Transport Research Centre, University of Technology Sydney, Sydney, Australia, is expressly recognised.

Appendix A. LBM-DEM Approach

The ${\Omega_\alpha}^{BGK}$, through which the momentum transfer occurs between the fluid particles when they collide, is given by (Bhatnagar et al., 1954):

$$ {\Omega_\alpha}^{BGK} = -\frac{\Delta t}{\tau}\left(f_\alpha(x,t) - {f_\alpha^{eq}}(x,t)\right) \tag{A.1} $$

where ${f_\alpha^{eq}}(x,t)$ is the equilibrium distribution function, τ is the relaxation time, and is related to the kinematic viscosity (ν_f) of the fluid, the lattice spacing (Δx), and the time step (Δt) by the following relationship:

$$ \nu_f = \frac{1}{3}\left(\tau - \frac{1}{2}\right)\frac{\Delta x^2}{\Delta t} \tag{A.2} $$

Eq. (A.2) implies that the τ value should be greater than 0.5. For a given value of ν_f and τ, the Δt is defined according to the chosen Δx by:

$$ \Delta t = \frac{1}{3\nu_f}\left(\tau - \frac{1}{2}\right)\Delta x^2 \tag{A.3} $$

The ${f_\alpha^{eq}}(x,t)$ for the BGK model is given by (Bhatnagar et al., 1954):

$$ {f_\alpha^{eq}}(x,t) = \omega_\alpha \rho_f \left(1 + \frac{3}{{c_L}^2} e_\alpha^v\, u + \frac{9}{2{c_L}^4}(e_\alpha^v\, u)^2 - \frac{3}{2{c_L}^2}u^2\right) \tag{A.4} $$

where, ω_α is the weighting factor for the velocity vectors, ρ_f is the fluid density, e_α^v is the microscopic fluid velocity, u is the macroscopic fluid velocity, and c_L is the lattice speed given by:

$$ c_L = \frac{\Delta x}{\Delta t} \tag{A.5} $$

In lattice Boltzmann computations, $c_L = \Delta x = \Delta t = 1$, and the discretisation schemes in LBM are labelled as *DdQq,* where *d* is the number of dimensions, and *q* represents the number of velocity vectors. This study used the *D3Q19*, a three-dimensional scheme with 19 velocity vectors, including one at rest. Figure A.1 shows the directions of the velocity vectors (e_α^v) for the *D3Q19* scheme and, for the sake of simplicity, their magnitudes are already defined by:

$$e_\alpha^v = \begin{cases} (0,0,0) & i = 0 \\ (\pm c_L, 0,0), (0, \pm c_L, 0), (0,0, \pm c_L) & i = 1,2,3,4,5,6 \\ (\pm c_L, \pm c_L, 0), (\pm c_L, 0, \pm c_L), (0, \pm c_L, \pm c_L) & i = 7,8,9,10,11, \dots, 18 \end{cases} \tag{A.6}$$

and the weighing factors are $\omega_0 = 1/3$, $\omega_{1,2,3,4,5,6} = 1/18$ and $\omega_{7,8,\dots,18} = 1/36$.

The macroscopic fluid properties, i.e., fluid density (ρ_f) and velocity (u) can be retrieved at each node and given by (Han & Cundall, 2017; Seil et al., 2018):

$$\rho_f\,(x,t) = \sum_{\alpha=0}^{q-1} f_\alpha(x,t) \tag{A.7}$$

$$u\,(x,t) = \frac{1}{\rho_f} \sum_{\alpha=0}^{q-1} f_\alpha(x,t) e_\alpha^v \tag{A.8}$$

To determine the fluid pressure p_f, it is assumed that the fluid is slightly compressible, and the following state equation is used:

$$p_f = c_s^2 \rho_f \tag{A.9}$$

where c_s is the sound celerity and is defined by:

$$c_s = \frac{c_L}{\sqrt{3}} \tag{A.10}$$

Fluid modelled with LBM requires a slight variation in spatial density. An approximate incompressibility situation can only be achieved under the condition that the Mach number (M) is small; is therefore kept below 0.1 (Han et al., 2007), and is defined by:

$$M = \frac{u_{max}}{c_L} \tag{A.11}$$

u_{max} is the maximum velocity in the fluid flow in physical units. Fluids with lower viscosity and turbulent flows can also be simulated with LBM using the Smagorinsky Large Eddy Simulation approach (Han et al., 2007; Seil et al., 2018).

For the fluid-particle interaction, the force (f_f) (without the static buoyancy force) and the torque (T_f) acting on a particle through the fluid can then be computed by (Noble & Torczynski, 1998; Seil et al., 2018):

$$f_f = \frac{\Delta x^3}{\Delta t}\left[\sum_n B_n \sum_\alpha {\Omega_\alpha}^s e_\alpha^v\right] \tag{A.12}$$

$$T_f = \frac{\Delta x^3}{\Delta t}\left[\sum_n B_n \left(x^n - x^p\right) \sum_\alpha {\Omega_\alpha}^s e_\alpha^v\right] \tag{A.13}$$

B_n is the weighting function in the cell, x^n is the coordinate of the lattice cell, and x^p is the centre of mass of the particle. Eq. (A.12) does not include the static buoyancy forces; therefore, they are applied separately to the particles and the total hydrodynamic force (f_{hyd}) on the particle, including the static buoyancy force (f_{bu}) is given by:

$$f_{hyd} = f_f + f_{bu} \tag{A.14}$$

The governing equations of motion of solid particles given by Cundall & Strack (1979), with the additional fluid-particle interaction force and the torque, are as follows:

$$m^p \frac{dv^p}{dt} = f_g^p + f_{hyd}^p + \sum_{c=1}^{N_c^p} f_j^c \qquad (A.15)$$

$$I^p \frac{dw^p}{dt} = T_f^p + \sum_{c=1}^{N_c^p} T_j^c \qquad (A.16)$$

where m^p and I^p are the mass and the moment of inertia of the particle p, v^p and w^p are the translational and angular velocities of the particle p, N_c^p is the total number of contacts on the particle p, f_j^c is the contact force vector in the j^{th} direction at contact c on the particle p, T_j^c is the torque that acts on the particle p due to the tangential contact force at contact c, and f_g^p is the gravitational force on the particle p.

Appendix B. Hertz-Mindlin Contact Model

Figure B.1 shows the rheological scheme and schematic sketch of the Hertz-Mindlin contact model used in this study to simulate the fluidisation of the soil. The normal contact force (f^N) is based on Hertzian contact theory and the tangential contact force (f^T) is based on the work of Mindlin & Deresiewicz (1989). The f^N and f^T have the nonlinear spring and damping components. The normal and tangential damping coefficients (c_n and c_t) are related to the restitution coefficient as reported by Tsuji et al. (1992). The tangential frictional force follows Coulomb's friction law (e.g., Cundall & Strack, 1979).

$$f^N = k_n \delta_n - c_n v_n^{rel} \qquad (B.1)$$

where k_n is the elastic constant for normal contact, c_n is the viscoelastic damping constant for normal contact, δ_n is the normal component of the displacement at the contact as represented by the overlap distance, v_n^{rel} is the normal component of the relative velocity of two spherical particles, and k_n is given by:

$$k_n = \frac{4}{3}E^*\sqrt{R^*\delta_n} \tag{B.2}$$

where E^* is the equivalent Young's modulus and R^* is the equivalent radius which can be written as follows:

$$\frac{1}{R^*} = \frac{1}{R_i} + \frac{1}{R_j} \tag{B.3}$$

$$\frac{1}{E^*} = \frac{1 - \nu_i^2}{E_{y_i}} + \frac{1 - \nu_j^2}{E_{y_j}} \tag{B.4}$$

where R_i and R_j are the radius, E_{y_i} and E_{y_j} are Young's modulus, and ν_i and ν_j are the Poisson's ratio of each neighbouring spheres in contact. The viscoelastic damping constant (c_n) is given by:

$$c_n = -2\sqrt{\frac{5}{6}}\ \beta\sqrt{S_n\, m^*} \quad \geq 0 \tag{B.5}$$

where, m^* is the equivalent mass and is given by:

$$\frac{1}{m^*} = \frac{1}{m_i} + \frac{1}{m_j} \tag{B.6}$$

β and S_n are given by:

$$\beta = \frac{ln\, e_r}{\sqrt{ln^2 e_r + \pi^2}} \tag{B.7}$$

$$S_n = 2E^*\sqrt{R^*\delta_n} \tag{B.8}$$

where e_r is the coefficient of restitution. The tangential contact force (f^T) is given by:

$$f^T = k_t\delta_t - c_t v_t^{rel} \tag{B.9}$$

where k_t is the elastic constant for tangential contact, c_t is the viscoelastic damping constant for tangential contact, δ_t is the tangential overlap, and v_t^{rel} is the tangential component of the relative velocity of two spherical particles, and k_t is given by:

$$k_t = 8G^* \sqrt{R^* \delta_n} \tag{B.10}$$

with G^* as the equivalent shear modulus, and c_t is written as follows:

$$c_t = -2\sqrt{\frac{5}{6}}\ \beta\sqrt{k_t\, m^*} \quad \geq 0 \tag{B.11}$$

The f^T is limited by:

$$f^T = \mu_s\, f^N \tag{B.12}$$

where μ_s is the coefficient of sliding friction.

Notations

The following symbols are used in this paper:

B = weighing function to correct the collision phase due to the presence of solid particles,

B_R = percentage of broken contacts,

c_L = lattice speed,

c_n = viscoelastic damping constant for normal contact,

c_s = sound celerity,

c_t = viscoelastic damping constant for tangential contact,

d_p = diameter of the particle,

d_{50} = particle size that is 50% finer by mass in the particle size distribution,

d_{85} = particle size that is 85% finer by mass in the particle size distribution,

E^* = equivalent Young's modulus,

e_α^v = microscopic fluid velocity,

e_{oi}^k = initial void ratio of the k^{th} layer,

e_{oi}^{avg} = initial void ratio of the entire sample considering all 10 Layers,

e_r = coefficient of restitution,

f_{bu} = static buoyancy force on the particle,

f_{hyd}^p = total hydrodynamic force (including the static buoyancy force) on the particle p,

f_f = hydrodynamic forces on the particle without buoyancy force,

f_g^p = gravitational force on the particle p,

f_j^c = force vector in j^{th} direction at contact c,

f^T = tangential contact force,

f^N = normal contact force,

$f_o^{N,avg}$ = average normal contact force in a layer at the hydrostatic state,

$f_\alpha(x,t)$ = particle distribution function,

$f_\alpha(x,t^*)$ = particle distribution function after the collision of fluid particles,

$f_\alpha^{eq}(x,t)$ = equilibrium distribution function,

G^* = equivalent shear modulus,

I^p = moment of inertia of the particle p,

i_o = overall applied hydraulic gradient,

$i_{o,cr}$ = critical overall hydraulic gradient of the soil specimen,

i_{hyd} = local hydraulic gradient in a layer,

k_n = elastic constant for normal contact,

k_t = elastic constant for tangential contact,

M = Mach number,

M_s = fraction of mechanically stable particles,

m^p = mass of the particle p,

m^* = equivalent mass,

N = lattice resolution,

N_c = number of contacts,

N_d = number of degrees of freedom,

N_{ct} = number of constraints,

N_c^p = number of contacts on particle p,

N_p = number of particles,

$N_p^{\geq 4}$ = number of particles with at least 4 or more contacts,

n = overall porosity of the soil specimen,

$n_i^{c,p}$ = unit-normal vector from the particle' centroid to the contact location,

n_L = number of layers,

O_i = initial centroidal location of particle i,

O_j = initial centroidal location of particle j,

O_j' = displaced centroidal location of particle j,

R = constraint ratio for a three-dimensional particle system with only sliding resistance,

R^* = equivalent radius,

Re_p = Reynold's number of the particle,

S = variance in the void ratios,

S_i = slipping index,

S_c = fraction of slipping contacts,

T_f^p= fluid-particle interaction torque,

T_j^c = interparticle contact torque due to tangential force,

t = time,

t^* = time after the collision,

u = macroscopic fluid velocity,

u_{max} = maximum velocity of the fluid flow in physical units,

V = volume of the selected region or layer,

V^p = volume of particle p,

v_d = superficial or discharge velocity of the fluid,

v_f = kinematic viscosity of fluid,

v_n^{rel} = normal component of the relative velocity of two spherical particles,

v_t^{rel}= tangential component of the relative velocity of two spherical particles,

v^p = translational velocity of the particle p,

w^p = angular velocity of the particle p,

ω_α = weighing factor for the microscopic fluid velocity,

x^n = coordinate of the lattice cell,

x_i^p = centre of mass of the particle,

z = location of the particle,

Z = coordination number,

$Z_{avg.}$ = average coordination number,

Δx = lattice spacing,

ρ_f = fluid density,

δ_n = normal overlap,

δ_t = tangential overlap,

Ω_α = collision operator,

${\Omega_\alpha}^{BGK}$ = collision operator of the BGK model,

${\Omega_\alpha}^{s}$ = additional collision term for solid fraction,

ε_s = solid fraction in the fluid cell volume,

τ = relaxation time,

μ_s = coefficient of sliding friction,

μ_f = dynamic viscosity of the fluid,

σ'_{ij} = Cauchy effective stress tensor in the selected region,

$\sigma_{ij}^{p\prime}$ = average stress tensor within a particle p,

σ'_{zz} = Cauchy effective stresses of the particles in a layer in the fluid flow direction at any time, and

σ'_{zzo} = initial Cauchy effective stresses of the particles in a layer in the fluid flow direction.

References

[1] Chawla S, Shahu JT. Reinforcement and mud-pumping benefits of geosynthetics in railway tracks: Model tests. Geotextiles and Geomembranes 2016; 44(3): 366-380. DOI: https://doi.org/10.1016/j.geotexmem.2016.01.005

[2] Duong TV, Cui Y-J, Tang AM, Dupla J-C, Canou J, Calon N, Robinet A. Investigating the mud pumping and interlayer creation phenomena in railway sub-structure. Engineering Geology 2014; 171: 45-58. DOI: https://doi.org/10.1016/j.enggeo.2013.12.016

[3] Hudson A, Watson G, Le Pen L, Powrie W. Remediation of Mud Pumping on a Ballasted Railway Track. Procedia Engineering 2016; 143: 1043-1050. DOI: https://doi.org/10.1016/j.proeng.2016.06.103

[4] Indraratna B, Singh M, Nguyen TT, Leroueil S, Abeywickrama A, Kelly R, Neville T. Laboratory study on subgrade fluidization under undrained cyclic triaxial loading. Canadian Geotechnical Journal 2020; 57(11): 1767-1779. DOI: 10.1139/cgj-2019-0350

[5] Nguyen TT, Indraratna B. Rail track degradation under mud pumping evaluated through site and laboratory investigations. International Journal of Rail Transportation 2021: 1-28. DOI: https://doi.org/10.1080/23248378.2021.1878947

[6] Nguyen TT, Indraratna B, Kelly R, Phan NM, Haryono F. Mud pumping under railtracks: Mechanisms, Assessments and Solutions. Australian Geomechanics Journal 2019; 54(4): 59-80.

[7] Cundall PA, Strack ODL. A discrete numerical model for granular assemblies. Géotechnique 1979; 29: 47-65.

[8] O'Sullivan C. Particulate discrete element modelling: a geomechanics perspective. 2011, London: Spon Press (an imprint of Taylor & Francis).

[9] Zhang J, Chen X, Zhang J, Jitsangiam P, Wang X. DEM investigation of macro- and micro-mechanical properties of rigid-grain and soft-chip mixtures. Particuology 2021; 55: 128-139. DOI: https://doi.org/10.1016/j.partic.2020.06.002

[10] Thornton C. Numerical simulations of deviatoric shear deformation of granular media. Géotechnique 2000; 50(1): 43-53. DOI: 10.1680/geot.2000.50.1.43

[11] Fonseca J, O'Sullivan C, Coop MR, Lee PD. Quantifying the evolution of soil fabric during shearing using directional parameters. Geotechnique 2013; 63(6): 487-499.

[12] Cundall PA, Strack ODL. Modeling of Microscopic Mechanisms in Granular Material. In: Studies in Applied Mechanics. Jenkins J.T., Satake M., Editors. Elsevier; 1983. p. 137-149.

[13] Cui X, Li J, Chan A, Chapman D. Coupled DEM–LBM simulation of internal fluidisation induced by a leaking pipe. Powder Technology 2014; 254: 299-306. DOI: https://doi.org/10.1016/j.powtec.2014.01.048

[14] Mansouri M, Delenne JY, El Youssoufi MS, Seridi A. A 3D DEM-LBM approach for the assessment of the quick condition for sands. Comptes Rendus Mécanique 2009; 337(9): 675-681. DOI: https://doi.org/10.1016/j.crme.2009.09.010

[15] Wang X, Huang B, Tang Y, Hu T, Ling D. Microscopic mechanism and analytical modeling of seepage-induced erosion in bimodal soils. Computers and Geotechnics 2022; 141: 104527. DOI: https://doi.org/10.1016/j.compgeo.2021.104527

[16] Nguyen TT, Indraratna B. The energy transformation of internal erosion based on fluid-particle coupling. Computers and Geotechnics 2020; 121: 103475. DOI: https://doi.org/10.1016/j.compgeo.2020.103475

[17] Han Y, Cundall P. Verification of two-dimensional LBM-DEM coupling approach and its application in modeling episodic sand production in borehole. Petroleum 2017; 3(2): 179-189. DOI: https://doi.org/10.1016/j.petlm.2016.07.001
[18] Indraratna B, Phan NM, Nguyen TT, Huang J. Simulating Subgrade Soil Fluidization Using LBM-DEM Coupling. International Journal of Geomechanics 2021; 21(5): 04021039. DOI: doi:10.1061/(ASCE)GM.1943-5622.0001997
[19] Wang M, Feng YT, Pande GN, Chan AHC, Zuo WX. Numerical modelling of fluid-induced soil erosion in granular filters using a coupled bonded particle lattice Boltzmann method. Computers and Geotechnics 2017; 82: 134-143. DOI: https://doi.org/10.1016/j.compgeo.2016.10.006
[20] Han K, Feng YT, Owen DRJ. Coupled lattice Boltzmann and discrete element modelling of fluid–particle interaction problems. Computers & Structures 2007; 85(11): 1080-1088. DOI: https://doi.org/10.1016/j.compstruc.2006.11.016
[21] Rettinger C, Rüde U. A comparative study of fluid-particle coupling methods for fully resolved lattice Boltzmann simulations. Computers & Fluids 2017; 154: 74-89. DOI: https://doi.org/10.1016/j.compfluid.2017.05.033
[22] Seil P, Pirker S, Lichtenegger T. Onset of sediment transport in mono- and bidisperse beds under turbulent shear flow. Computational Particle Mechanics 2018; 5(2): 203-212. DOI: 10.1007/s40571-017-0163-6
[23] Skempton AW, Brogan JM. Experiments on piping in sandy gravels. Geotechnique 1994; 44(3): 449-460.
[24] Indraratna B, Israr J, Rujikiatkamjorn C. Geometrical method for evaluating the internal instability of granular filters based on constriction size distribution. Journal of Geotechnical and Geoenvironmental Engineering 2015; 141(10): 04015045. DOI: doi:10.1061/(ASCE)GT.1943-5606.0001343
[25] Tao H, Tao J. Quantitative analysis of piping erosion micro-mechanisms with coupled CFD and DEM method. Acta Geotechnica 2017; 12(3): 573-592. DOI: 10.1007/s11440-016-0516-y
[26] Fleshman MS, Rice JD. Laboratory modeling of the mechanisms of piping erosion initiation. Journal of Geotechnical & Geoenvironmental Engineering 2014; 140(6): 04014017:1-12.
[27] Chen S, Martínez D, Mei R. On boundary conditions in lattice Boltzmann methods. Physics of Fluids 1996; 8(9): 2527-2536. DOI: 10.1063/1.869035
[28] Bhatnagar PL, Gross EP, Krook M. A Model for Collision Processes in Gases. I. Small Amplitude Processes in Charged and Neutral One-Component Systems. Physical Review 1954; 94(3): 511-525. DOI: 10.1103/PhysRev.94.511
[29] Noble DR, Torczynski JR. A Lattice-Boltzmann Method for Partially Saturated Computational Cells. International Journal of Modern Physics C 1998; 09(08): 1189-1201. DOI: 10.1142/s0129183198001084
[30] Nguyen TT, Indraratna B. Hydraulic behaviour of parallel fibres under longitudinal flow: a numerical treatment. Canadian Geotechnical Journal 2016; 53(7): 1081-1092. DOI: https://doi.org/10.1139/cgj-2015-0213
[31] Cate At, Nieuwstad CH, Derksen JJ, Akker HEAVd. Particle imaging velocimetry experiments and lattice-Boltzmann simulations on a single sphere settling under gravity. Physics of Fluids 2002; 14(11): 4012-4025. DOI: 10.1063/1.1512918
[32] Abbireddy COR, Clayton CRI. Varying initial void ratios for DEM simulations. Géotechnique 2010; 60(6): 497-502. DOI: 10.1680/geot.2010.60.6.497
[33] Indraratna B, Haq S, Rujikiatkamjorn C, Israr J. Microscale boundaries of internally stable and unstable soils. Acta Geotechnica 2021. DOI: 10.1007/s11440-021-01321-7

[34] Senetakis K, Coop MR, Todisco MC. Tangential load–deflection behaviour at the contacts of soil particles. Géotechnique Letters 2013; 3(2): 59-66. DOI: 10.1680/geolett.13.00019

[35] Hu Z, Zhang Y, Yang Z. Suffusion-induced deformation and microstructural change of granular soils: a coupled CFD–DEM study. Acta Geotechnica 2019; 14(3): 795-814. DOI: 10.1007/s11440-019-00789-8

[36] Nguyen TT, Indraratna B. A coupled CFD-DEM approach to examine the hydraulic critical state of soil under increasing hydraulic gradient. ASCE International Journal of Geomechanics 2020; 20(9): 04020138-1:15. DOI: https://doi.org/10.1061/(ASCE)GM.1943-5622.0001782

[37] Huang X, Hanley KJ, O'Sullivan C, Kwok FCY. Effect of sample size on the response of DEM samples with a realistic grading. Particuology 2014; 15: 107-115. DOI: https://doi.org/10.1016/j.partic.2013.07.006

[38] Jiang MJ, Konrad JM, Leroueil S. An efficient technique for generating homogeneous specimens for DEM studies. Computers and Geotechnics 2003; 30(7): 579-597. DOI: https://doi.org/10.1016/S0266-352X(03)00064-8

[39] Terzaghi K. Theoretical soil mechanics. 1943, New York: John Wiley & Sons.

[40] Potyondy DO, Cundall PA. A bonded-particle model for rock. International Journal of Rock Mechanics and Mining Sciences 2004; 41(8): 1329-1364.

[41] Li M, Fannin RJ. A theoretical envelope for internal instability of cohesionless soil. Géotechnique 2012; 62(1): 77-80. DOI: 10.1680/geot.10.T.019

[42] Imole OI, Kumar N, Magnanimo V, Luding S. Hydrostatic and Shear Behavior of Frictionless Granular Assemblies under Different Deformation Conditions. KONA Powder and Particle Journal 2013; 30: 84-108. DOI: 10.14356/kona.2013011

LIST OF TABLES

Table 1. Fluid properties for simulating the single-particle falling into the fluid using the LBM-DEM approach (after Ten Cate et al. 2002).

LIST OF FIGURES

Fig. 1. Flowchart of the Lattice Boltzmann Method (LBM) combined with the Discrete Element Method (DEM).

Fig. 2. (a) Schematic representation of a single sphere falling into the fluid with a diameter (d_p) = 15 mm; (b) the modelled particle in the fluid mesh using LBM-DEM; (c) comparison of the numerical and experimental results of particle position over time; (d) comparison of experimental and numerical results of particle velocity over time.

Fig. 3. (a) Particle size distribution of the sample selected for modelling in DEM; (b) three-dimensional sample modelled in DEM; (c) division of the sample into different layers with the mentioned layer numbers and initial void ratios (e_{oi}); (d) a close-up view of the particles modelled in the fluid mesh using the LBM-DEM approach.

Fig. 4. Calibration of the soil specimen fluidisation model by comparing the flow curves obtained from the LBM-DEM and the documented experimental work.

Fig. 5. Evolution of the local hydraulic gradient (i_{hyd}) and the normalised effective stresses ($\sigma'_{zz}/\sigma'_{zzo}$).

Fig. 6. Evolution of broken contacts (B_R) with the normalised effective stresses ($\sigma'_{zz}/\sigma'_{zzo}$).

Fig. 7. Development of the fraction of mechanically stable particles (M_s) with normalised effective stresses ($\sigma'_{zz}/\sigma'_{zzo}$).

Fig. 8. Conceptual model showing the differences in the fabrics of particles with the same void ratios.

Fig. 9. Distributions of the coordination number (*Z*) at the hydrostatic state and the onset of fluidisation of soil specimen.

Fig. 10. Development of the average coordination number (Z_{avg}) with normalised effective stresses ($\sigma'_{zz}/\sigma'_{zzo}$).

Fig. 11. Distribution of the slipping index (S_i) of the selected Layer 10 with different local hydraulic gradients (i_{hyd}).

Fig. 12. (a) Three-dimensional representation of the hydraulic gradient (i_{hyd}), the normalised effective stresses ($\sigma'_{zz}/\sigma'_{zzo}$), and the constraint ratio *(R*); (b) projections of the three-dimensional plot of i_{hdy}, $\sigma'_{zz}/\sigma'_{zzo}$, and *R*.

Fig. A1. Directions of the 19 (0-18) velocity vectors of the *D3Q19* discretisation scheme used in this study.

Fig. A2. (a) Rheological scheme and (b) schematic sketch of the Hertz-Mindlin contact model used in this study to simulate fluidisation of soil specimen.

Table 1. Fluid properties for simulating the single-particle falling into the fluid using the LBM-DEM approach (after Ten Cate et al. 2002)

Case	**Density (ρ_f) (kg/m^3)**	**Kinematic Viscosity (υ_f) (m^2/s)**
Re_p = 1.5	970	3.845 x 10^{-4}
Re_p = 4.1	965	2.197 x 10^{-4}
Re_p = 11.6	962	1.175 x 10^{-4}
Re_p = 31.9	960	6.042 x 10^{-5}

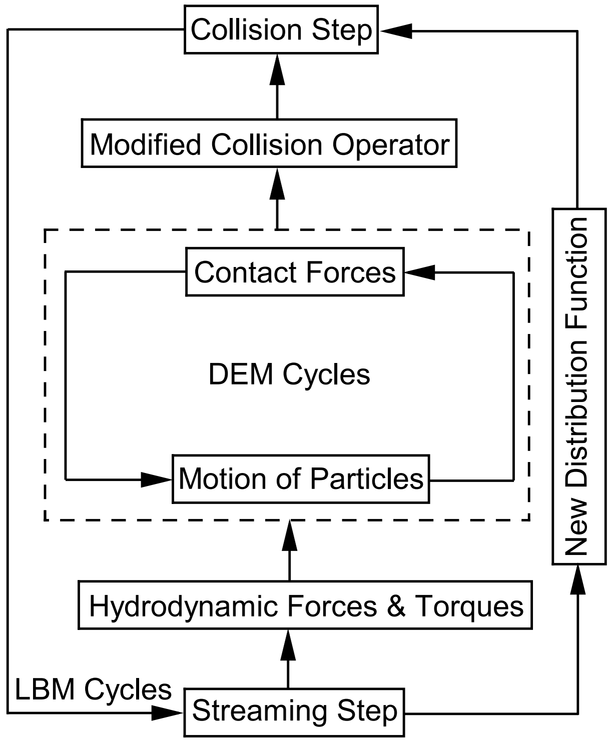

Fig. 1. Flowchart of the Lattice Boltzmann Method (LBM) combined with the Discrete Element Method (DEM)

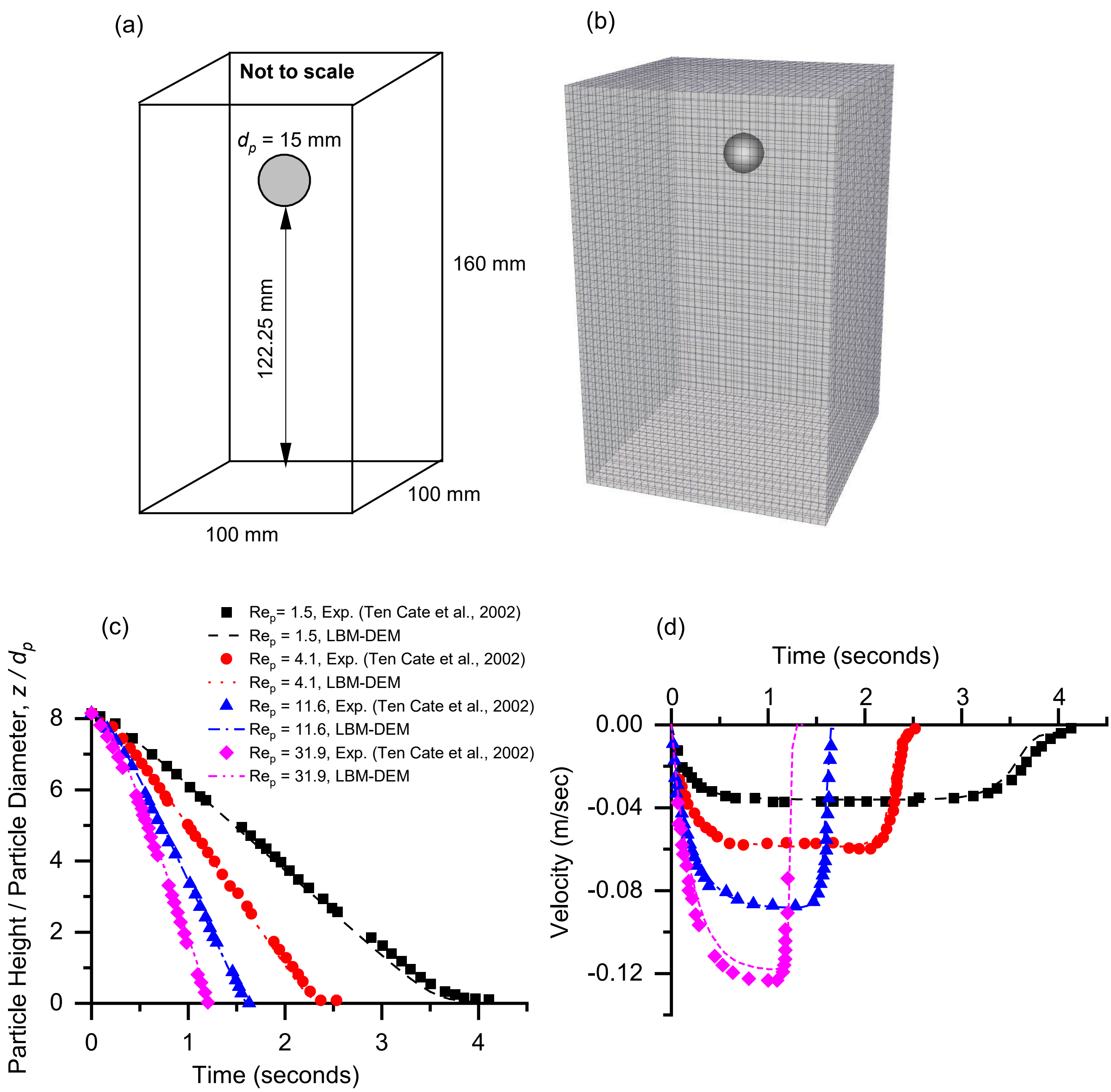

Fig. 2. (a) Schematic representation of a single sphere falling into the fluid with a diameter (d_p) = 15 mm; (b) the modelled particle in the fluid mesh using LBM-DEM; (c) comparison of the numerical and experimental results of particle position over time; (d) comparison of experimental and numerical results of particle velocity over time

Fig. 3.

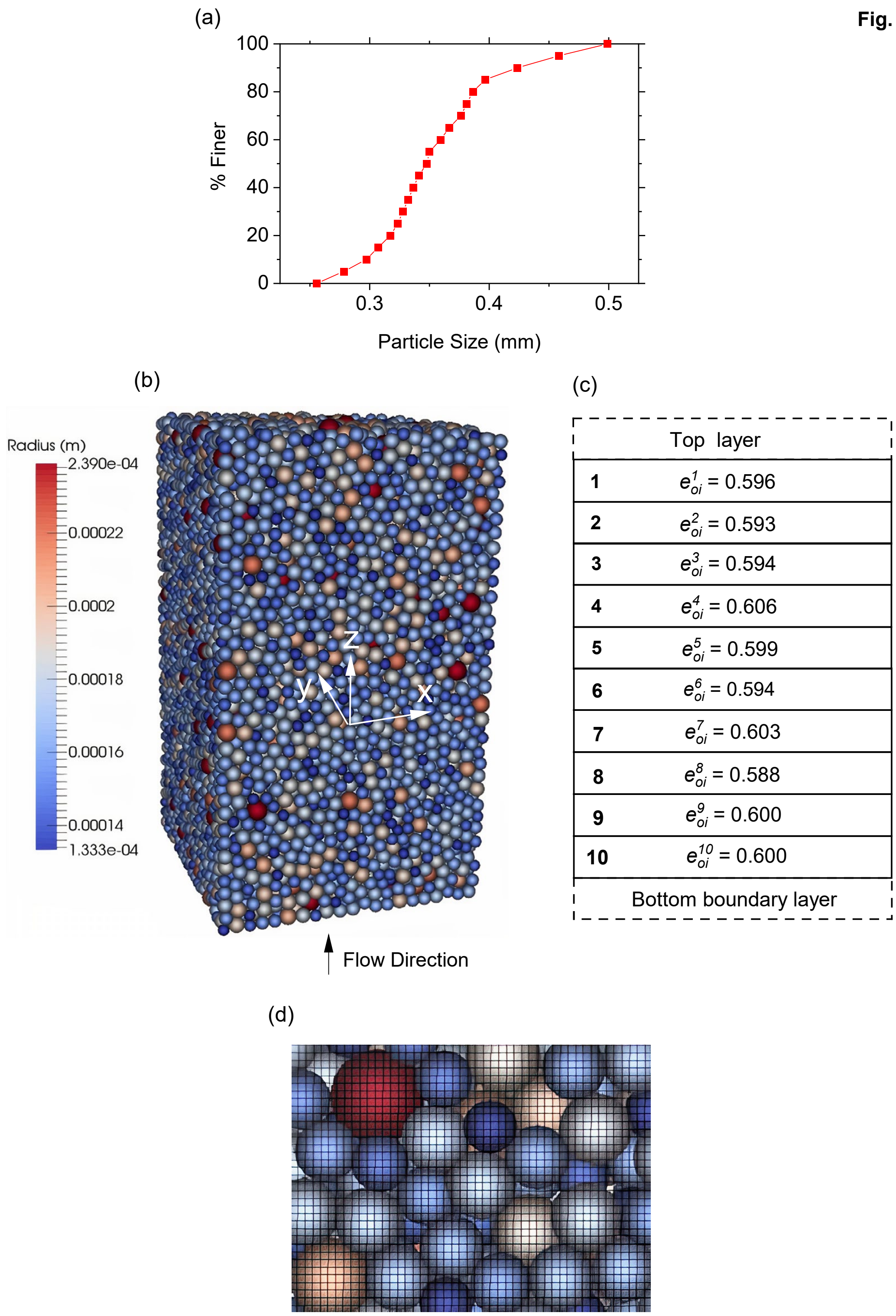

Fig. 3. (a) Particle size distribution of the sample selected for modelling in DEM; (b) three-dimensional sample modelled in DEM; (c) division of the sample into different layers with the mentioned layer numbers and initial void ratios (e_{oi}); (d) a close-up view of the particles modelled in the fluid mesh using the LBM-DEM approach

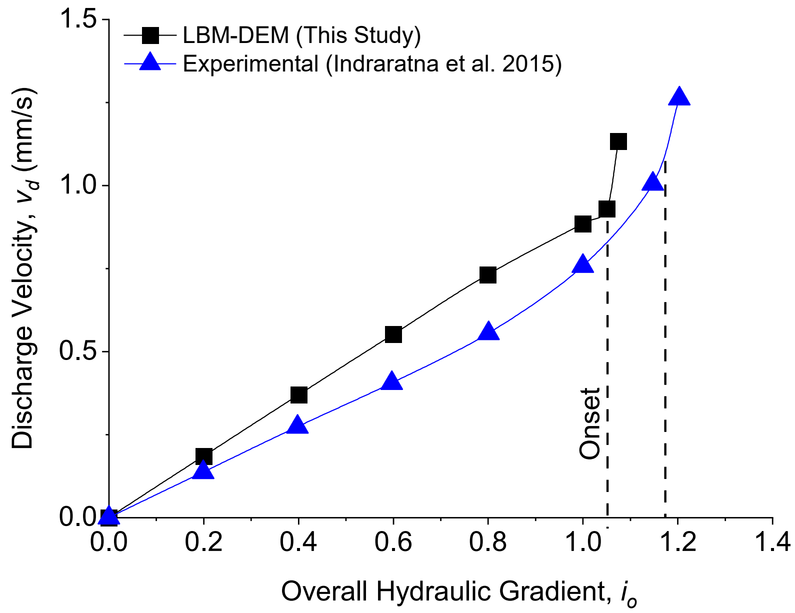

Fig. 4. Calibration of the soil specimen fluidisation model by comparing the flow curves obtained from the LBM-DEM and the documented experimental work

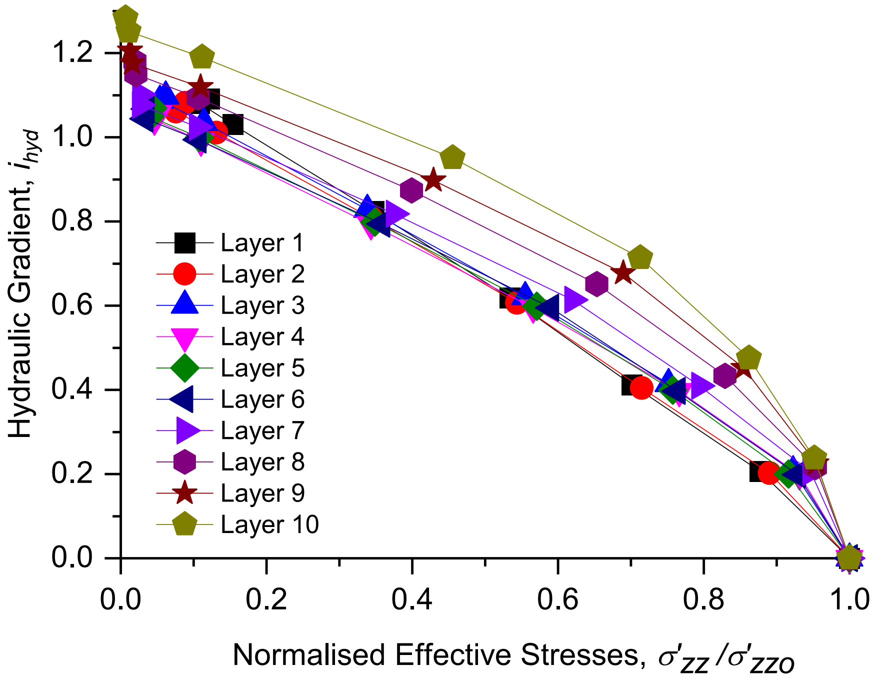

Fig. 5. Evolution of the local hydraulic gradient (i_{hyd}) and the normalised effective stresses ($\sigma'_{zz}/\sigma'_{zzo}$)

773

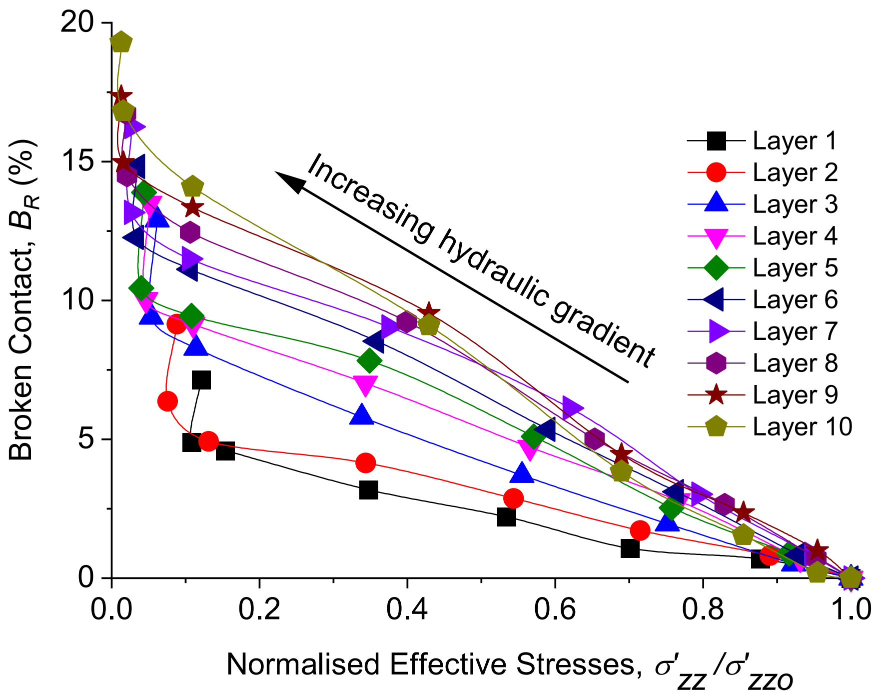

774 **Fig. 6.** Evolution of broken contacts (B_R) with the normalised effective stresses ($\sigma'_{zz}/\sigma'_{zzo}$)

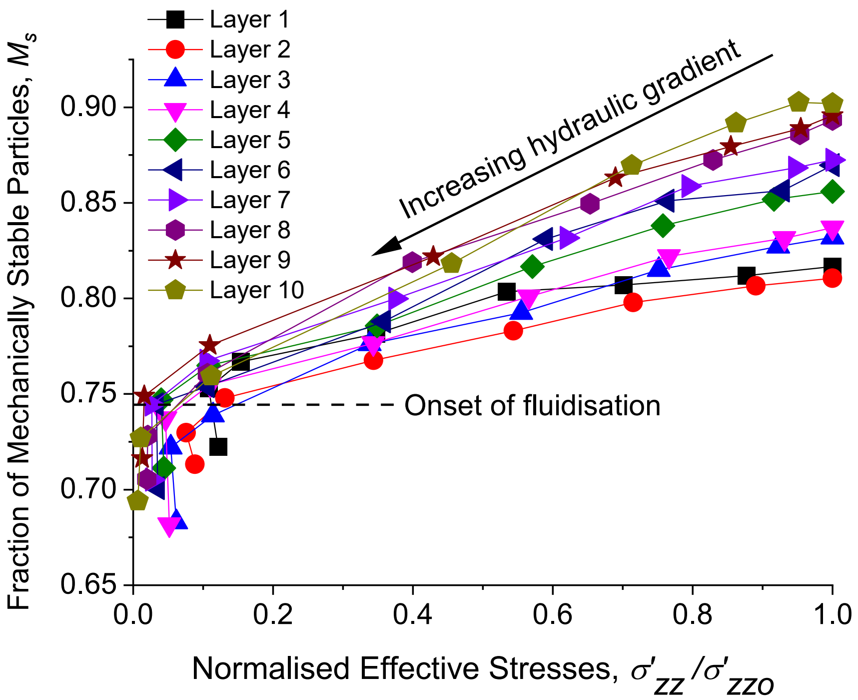

Fig. 7. Development of the fraction of mechanically stable particles (M_s) with normalised effective stresses ($\sigma'_{zz}/\sigma'_{zzo}$)

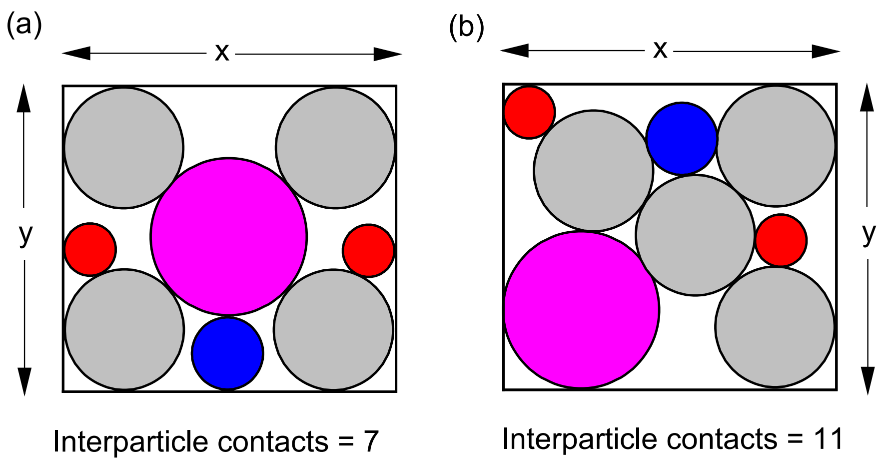

Fig. 8. Conceptual model showing the differences in the fabrics of particles with the same void ratios

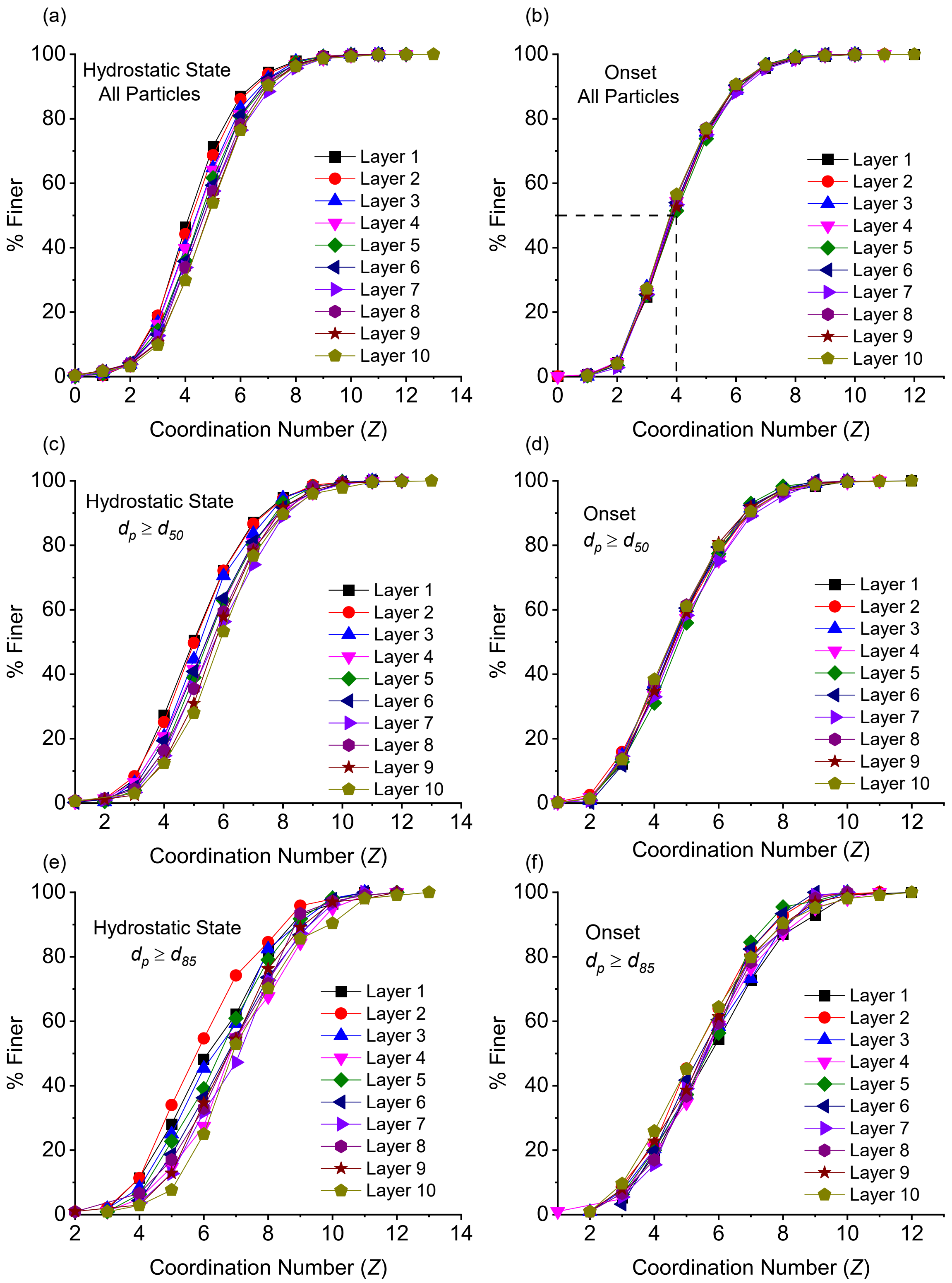

Fig. 9. Distributions of the coordination number (Z) at the hydrostatic state and the onset of fluidisation of soil specimen

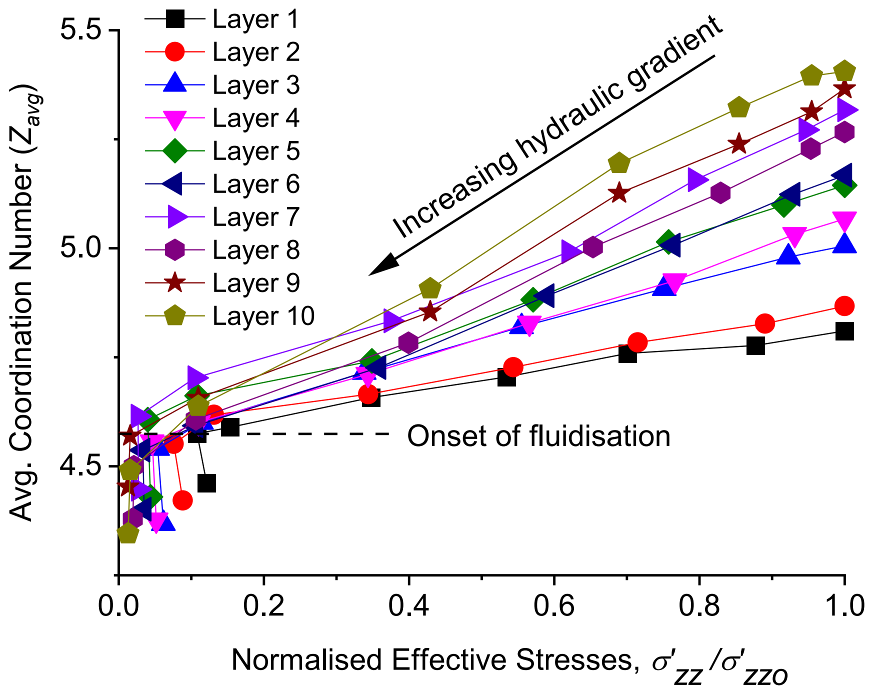

Fig. 10. Development of the average coordination number (Z_{avg}) with normalised effective stresses ($\sigma'_{zz}/\sigma'_{zzo}$)

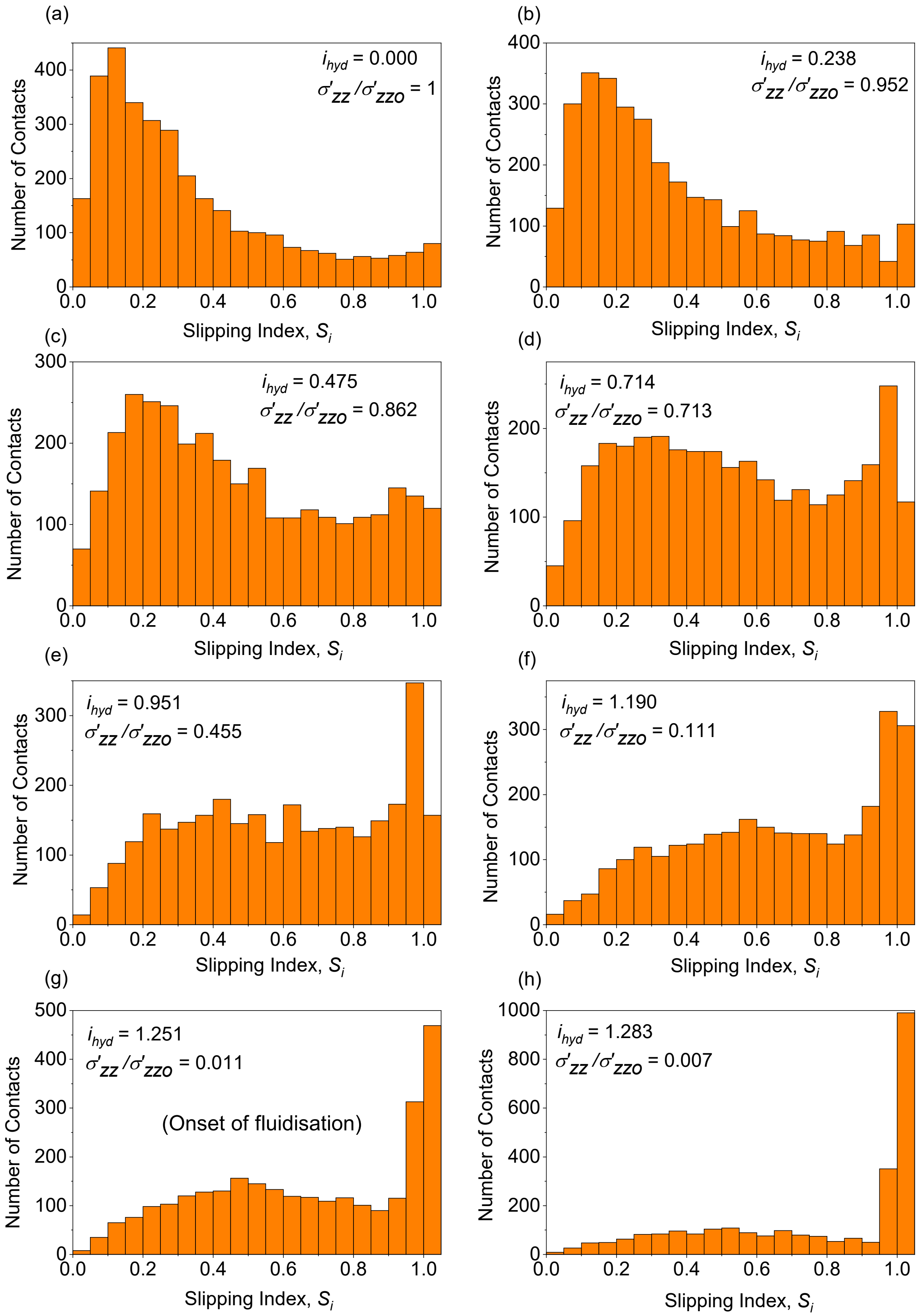

Fig. 11. Distribution of the slipping index (S_i) of the selected Layer 10 with different local hydraulic gradients (i_{hyd})

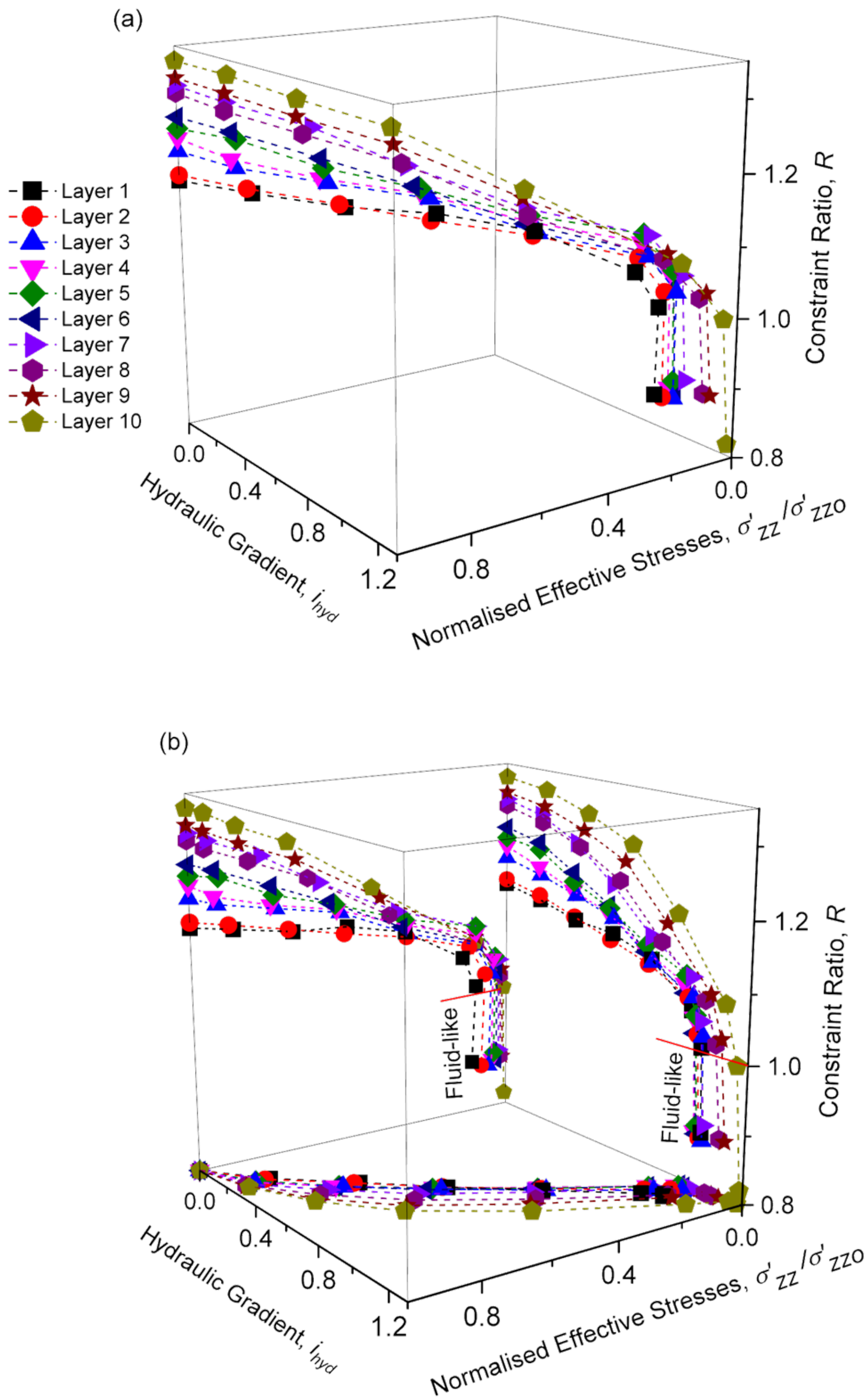

Fig. 12. (a) Three-dimensional representation of the hydraulic gradient (i_{hyd}), the normalised effective stresses ($\sigma'_{zz}/\sigma'_{zzo}$), and the constraint ratio *(R)*; (b) projections of the three-dimensional plot of i_{hdy}, $\sigma'_{zz}/\sigma'_{zzo}$, and *R*.

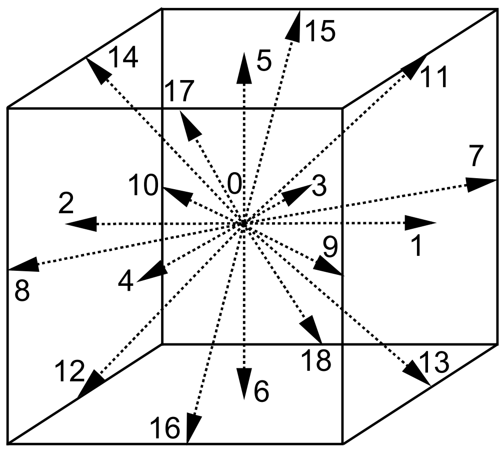

Fig. A.1. Directions of the 19 (0-18) velocity vectors of the *D3Q19* discretisation scheme used in this study

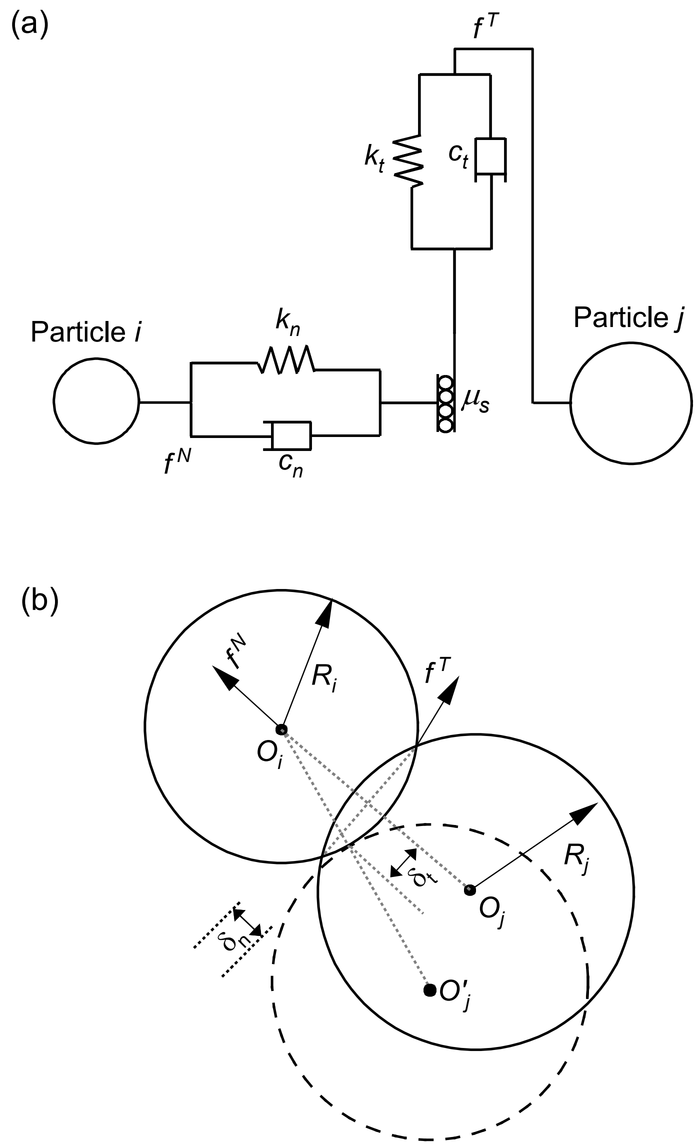

Fig. A.2. (a) Rheological scheme and (b) schematic sketch of the Hertz-Mindlin contact model used in this study to simulate fluidisation of soil specimen